Understanding ENSO variability and its extrema: A delay differential equation approach

Michael Ghil* and Ilya Zaliapin†

August 13, 2009

Abstract

We review and analyze in further detail a simple model of El-Niño/Southern-Oscillation (ENSO) variability. The model is formulated as a forced delay differential equation for sea surface temperature T in the Tropical Pacific, and it combines two key mechanisms that participate in ENSO dynamics: delayed negative feedback and seasonal forcing. This model's rich behavior is studied via stability and bifurcation analyses in the three-dimensional space of its physically relevant parameters: strength of seasonal forcing b, atmosphere-ocean coupling κ, and propagation period τ of oceanic waves across the Tropical Pacific.

Two regimes of variability, stable and unstable, are reported; they are separated by a sharp neutral curve in the (b, τ) plane at constant κ. The detailed structure of the neutral curve becomes very irregular and possibly fractal, while individual trajectories within the unstable region become highly complex and possibly chaotic, as the atmosphere–ocean coupling κ increases. In the unstable regime, spontaneous transitions occur in the mean T, period, and extreme annual values, given purely periodic, seasonal forcing.

The model's behavior exhibits phase locking to the seasonal cycle, namely the local maxima and minima of T tend to occur at the same time of year; this locking is a characteristic feature of the observed El Niño (warm) and La Niña (cold) events. Multiple model solutions co-exist and we describe their basins of attraction. We

---

*Geosciences Department and Laboratoire de Météorologie Dynamique (CNRS and IPSL), Ecole Normale Supérieure, Paris, FRANCE, and Department of Atmospheric & Oceanic Sciences and Institute of Geophysics & Planetary Physics, University of California, Los Angeles, USA. E-mail: ghil@atmos.ucla.edu.

†Department of Mathematics and Statistics, University of Nevada, Reno, USA. E-mail: zal@unr.edu.

expect similar behavior in much more detailed and realistic models, where it is harder to describe its causes as completely.

1 Introduction and motivation

1.1 Key ingredients of ENSO theory

The El-Niño/Southern-Oscillation (ENSO) phenomenon is the most prominent signal of seasonal-to-interannual climate variability. It was known for centuries to fishermen along the west coast of South America, who witnessed a seemingly sporadic and abrupt warming of the cold, nutrient-rich waters that support the food chain in those regions; these warmings caused havoc to their fish harvests [11, 40]. The common occurrence of such warming shortly after Christmas inspired them to name it El Niño, after the "Christ child." Starting in the 1970s, researchers found that El Niño's climatic effects were far broader than just its manifestations off the shores of Peru [11, 21]. This realization led to a global awareness of ENSO's significance, and triggerred an increased interest in modeling and forecasting exceptionally strong El Niño events [29].

Nonlinear and complex phenomena like ENSO require a full hierarchy of models for their study, from "toy" via intermediate to fully coupled general circulation models (GCMs) [18, 37]. We focus here on a "toy" model, which captures a qualitative, conceptual picture of ENSO dynamics that includes a surprisingly full range of features. This approach allows one to achieve a rather comprehensive understanding of the model's, and maybe the phenomenon's, underlying mechanisms and their interplay.

The following conceptual elements have been shown to play a determining role in the dynamics of the ENSO phenomenon.

(i) The Bjerknes hypothesis: Bjerkness [5], who laid the foundation of modern ENSO research, suggested a *positive feedback* as a mechanism for the growth of an internal instability that could produce large positive anomalies[1] of sea surface temperatures (SSTs) in the eastern Tropical Pacific. Using observations from the International Geo-

---

[1]In the atmospheric, oceanic and climate sciences, an *anomaly* is simply the difference between the instantaneous, or mean-monthly, value of a variable and its long-term "normal," *i.e.* its climatological mean.

physical Year (1957-1958), Bjerknes realized that this mechanism must involve *air-sea interaction* in the tropics.

The "chain reaction" starts with an initial warming of SSTs in the "cold tongue" that occupies the eastern part of the equatorial Pacific. This warming causes a weakening of the thermally direct Walker-cell circulation; this circulation involves air rising over the warmer SSTs near Indonesia and sinking over the colder SSTs near Peru. As the trade winds blowing from the east weaken and thus give way to westerly wind anomalies, the ensuing local changes in the ocean circulation encourage further SST increase. Thus the feedback loop is closed and further amplification of the instability is triggered. A schematic diagram of the atmospheric and oceanic circulation in the Tropical Pacific is shown in Fig. 1.

(ii) Delayed oceanic wave adjustments: Compensating for Bjerknes's positive feedback is a *negative feedback* in the system that allows a return to colder conditions in the basin's eastern part [43]. During the peak of the cold-tongue warming, called the *warm* or *El Niño* phase of ENSO, westerly wind anomalies prevail in the central part of the basin. As part of the ocean's adjustment to this atmospheric forcing, a Kelvin wave is set up in the tropical wave guide and carries a warming signal eastward; this signal deepens the eastern-basin thermocline, which separates the warmer, well-mixed surface waters from the colder waters below, and thus contributes to the positive feedback described above. Concurrently, slower Rossby waves propagate westward, and are reflected at the basin's western boundary, giving rise therewith to an eastward-propagating Kelvin wave that has a cooling, thermocline-shoaling effect. Over time, the arrival of this signal erodes the warm event, ultimately causing a switch to a *cold, La Niña* phase.

(iii) Seasonal forcing: A growing body of work [8, 9, 18, 26, 27, 45, 46] points to resonances between the Pacific basin's intrinsic air-sea oscillator and the annual cycle as a possible cause for the tendency of warm events to peak in boreal winter, as well as for ENSO's intriguing mix of temporal regularities and irregularities. The mechanisms by which this interaction takes place are numerous and intricate and their relative importance is not yet fully understood [2, 46].

The past 30 years of research have shown that ENSO dynamics is governed, by and large, by the interplay of the above nonlinear mechanisms and that their simplest version can be studied in autonomous or forced delay differential equation (DDE) models [3, 43, 45]. These DDE models follow their use in paleoclimate studies [4], provide a convenient paradigm for explaining interannual ENSO variability, and shed new light on its dynamical properties.

So far, though, DDE model studies of ENSO have been limited to linear stability analysis of steady-state solutions, which are not typical in forced systems; case studies of particular trajectories; or one-dimensional scenarios of transition to chaos, where one varies a single parameter while the others are kept fixed. A major obstacle for the complete bifurcation and sensitivity analysis of DDE models lies in the complex nature of these models, whose numerical and analytical treatment is considerably harder than that of systems of ordinary differential equations (ODEs).

Ghil *et al.*[20] took several steps toward a comprehensive analysis, numerical as well as theoretical, of a DDE model relevant to ENSO phenomenology. In doing so, they also illustrated the complexity of phase–parameter-space structure for even such a simple model of climate dynamics. Specifically, the authors formulated a toy DDE model for ENSO variability and focused on analysis of model solutions in a broad three-dimensional (3-D) domain of its physically relevant parameters. They showed that the model can reproduce many scenarios relevant to the ENSO phenomenology, including prototypes of warm and cold events, interdecadal oscillations, and even intraseasonal activity reminiscent of Madden-Julian oscillations or westerly-wind bursts.

The model was also able to provide a good justification for the observed quasi-biennial oscillation in Tropical Pacific sea-surface temperatures (SSTs) and trade winds [11, 17, 25, 40]. The most important finding of Ghil and coauthors [20] was the existence of regions of stable and unstable solution behavior in the model's parameter space; these regions have a complex and possibly fractal geometric structure. Interestingly, the values of the model parameters that correspond to actual ENSO dynamics lie on the border between the stable and unstable regions in this space. Hence, if the dynamical phenomena found in the model have any relation to reality, SSTs in the Tropical Pacific are expected to have an intrinsically unstable behavior.

The present paper briefly reviews the results of Ghil *et al.* [20] and pursues their DDE model analysis by focusing now on multiple model solutions for the same parameter values and on the dynamics of *local extrema*. The paper is organized as follows. Section 2 introduces the DDE model of ENSO variability, reviews the main theoretical results concerning its solutions, and comments on the appropriate numerical integration methods. Our novel results are reported and illustrated in Sect. 3. An overall discussion concludes the paper in Sect. 4.

4

2 Model and numerical integration method

2.1 Model formulation and parameters

Ghil *et al.* [20] studied the nonlinear DDE with additive, periodic forcing:

$$\frac{dh(t)}{dt} = -a \, \tanh\left[\kappa \, h(t - \tau)\right] + b \, \cos(2\pi \, \omega \, t). \tag{1}$$

Here $t \geq 0$ and the parameters a, κ, τ, b, and ω are all real and positive. Equation (1) mimics two mechanisms essential for ENSO variability: delayed negative feedback via the highly nonlinear function $\tanh(\kappa \, z)$ and periodic external forcing. It is inspired by, and further simplifies, earlier DDE models of ENSO [3, 43, 45]; these DDE models, in turn, were based on either fundamental physical considerations or on simplifications of intermediate ENSO models, such as [48].

The function $h(t)$ in (1) represents the thermocline depth anomalies, *i.e.*, its deviations from the annual mean in the Eastern Pacific. Accordingly, h can also be interpreted roughly as the regional SST anomaly, since a deeper thermocline corresponds to less upwelling of cold waters, and hence higher SST, and vice versa; see again Fig. 1. The thermocline depth is affected by the wind-forced, eastward Kelvin and westward Rossby oceanic waves. The waves' delayed effects are modeled by the function $\tanh\left[\kappa \, h(t - \tau)\right]$; the delay τ is due to the finite wave velocity and corresponds roughly to the combined basin-transit time of the Kelvin and Rossby waves. The forcing term represents the seasonal cycle in the trade winds.

The model (1) is fully determined by its five parameters: feedback delay τ, atmosphere-ocean coupling strength κ, feedback amplitude a, forcing frequency ω, and forcing amplitude b. By an appropriate rescaling of time t and dependent variable h, we let $\omega = 1$ and $a = 1$. The other three parameters may vary, reflecting different physical conditions of ENSO evolution. We consider here the following ranges of these parameters: $0 \leq \tau \leq 2$ yr, $0 < \kappa < \infty$, and $0 \leq b < \infty$.

To completely specify the DDE model (1) we need to prescribe some initial "history," *i.e.* the behavior of $h(t)$ on the interval $[-\tau, 0)$ [22]. Unless explicitly stated otherwise, we assume $h(t) \equiv 1$, $-\tau \leq t < 0$, *i.e.* we start with a warm year. Numerical experiments with alternative specifications of the initial history suggest that this choice does not affect our qualitative conclusions. In Sect. 3.4, though, we examine the multiplicity of solutions that arises from distinct intial histories.

2.2 Main theoretical result

Consider the function space $X = C([-\tau, 0), \mathbb{R})$ of continuous functions h from the initial interval $[-\tau, 0)$ to the real axis $\mathbb{R}$, $h : [-\tau, 0) \to \mathbb{R}$. Equiped with the norm for $h \in X$ given by

$$\| h \| = \sup \{|h(t)|, \ t \in [-\tau, 0)\},$$

X becomes a Banach space; here $| \cdot |$ denotes the absolute value in $\mathbb{R}$ [22, 39]. For convenience, we reformulate the DDE initial-value problem (IVP) in its rescaled form:

$$\frac{dh(t)}{dt} = -\tanh[\kappa \, h(t - \tau)] + b \, \cos(2\pi \, t), \ t \geq 0, \tag{2}$$

$$h(t) = \phi(t) \ \text{for} \ t \in [-\tau, 0), \quad \phi(t) \in X. \tag{3}$$

Ghil *et al.* [20] prove the following result.

Proposition 1 (Existence, uniqueness, continuous dependence) *For any fixed triplet of positive parameters (τ, κ, b), the IVP governed by Eqs. (2) and (3) has a unique solution $h(t)$ on $[0, \infty)$. This solution depends continuously on the initial data $\phi(t)$, delay τ and the right-hand side of (2) considered as a continuous map $f : [0, T) \times X \to \mathbb{R}$, for any finite time T.*

From Proposition 1 it follows, in particular, that the IVP (2)-(3) has a unique solution for all time, which depends continuously on the model parameters (τ, κ, b) and initial history $\phi(t)$ for any finite time. This result implies that any discontinuity in the solution profile as a function of the model parameters or history indicates existence of an unstable solution that separates the attractor basins of two stable solutions [20].

2.3 Numerical integration

The results in this study are based on numerical integration of the DDE (2) with initial data (3). We emphasize that there are important differences between the numerical integration of DDEs and ODEs. These differences require development of special software for DDEs, often accompanied by the problem-specific modification of such software. We used here the Fortran 90/95 DDE solver `dde_solver` of Shampine and Thompson ([42]), available at `http://www.radford.edu/~thompson/ffddes/`. Technical details of `dde_solver`, as well as a brief overview of other available DDE solvers are given in [20].

3   Results

3.1   Examples of model dynamics

This subsection illustrates typical solutions of our DDE model and comments on physically relevant aspects of these solutions. Figure 2 shows six model trajectories. Panel (a) ($\kappa = 5$, $\tau = 0.65$) illustrates the occurrence of "low-h," or cold, events every fourth seasonal cycle. Note that negative values of h correspond to the boreal (Northern Hemisphere) winter, that is to the upwelling season — December-January-February — in the eastern Tropical Pacific; in the present, highly idealized model, we can associate the extreme negative values with large-amplitude cold events, or La Niñas. This solution pattern loses its regularity when the atmosphere-ocean coupling increases: Panel (b) ($\kappa = 100, \tau = 0.58$) shows irregular occurrence of large cold events with the interevent time varying from 3 to 7 cycles.

In panel (c) ($\kappa = 50, \tau = 0.42$) we observe alternately and irregularly occurring warm El Niño and cold La Niña events: the "high-h" events occur with a period of about 4 years and random magnitude. Panel (d) ($\kappa = 500, \tau = 0.005$) shows another interesting type of behavior: bursts of intraseasonal oscillations of random amplitude superimposed on regular, period-one dynamics. This pattern is reminiscent of Madden-Julian oscillations [31, 32, 33] or of westerly-wind bursts [6, 10, 15, 23, 30, 41, 47]. Westerly wind bursts are physically related to atmospheric convection that is not a part of the current model. The somewhat surprising model result of high-frequency, intraseasonal variability suggests that realistic bursts might be excited in the atmosphere by or interact synergistically with the apparently slower mechanisms represented by this coupled model: they could be triggered by, rather than trigger, warm or cold ENSO episodes.

The solution in panel (e) ($\kappa = 50, \tau = 0.508$) demonstrates sustained interdecadal variability in the absence of any external source of such variability. The solution pattern illustrates spontaneous changes in the long-term annual mean, as well as in the distribution of positive and negative extremes, with respect to both time and amplitude.

3.2   Onset of the instabilities

Munnich *et al.* [36] and Tziperman *et al.* [45] reported that the onset of chaotic behavior in their ENSO models is associated with the increase of the atmosphere-ocean coupling κ. We explore this transition to chaos in our model over its entire, 3-D parameter space.

First, we compute in the three panels of Fig. 3 the trajectory maximum M as a

function of the parameters b and τ for values of κ that increase from the top to the bottom panel. For small values of coupling (top panel) we have a smooth map, monotonously increasing in b and periodic with period 1 in τ. As the coupling increases, the map loses its monotonicity in b and periodicity in τ for large values of τ, but it is still smooth. For $\kappa \approx 2$ (middle panel), a neutral curve $f(b, \tau) = 0$ emerges that separates a smooth region (to the right of the curve), where we still observe monotonicity in b and periodicity in τ, from a region with rough behavior of M. The gradient of $M(b, \tau)$ is quite sharp across this neutral curve.

Further increase of the coupling results in a qualitative change in the maximum map. The neutral curve, which becomes sharp and rough, separates two regions with very different behavior of $M(b, \tau)$ (bottom panel). To the right of the curve, the map $M(b, \tau)$ is still smooth, periodic in τ and monotonic in b. To the left, one sees discontinuities that produce rough and complicated patterns. The mean position of the neutral curve $f(b, \tau) = 0$ quickly converges to a fixed profile, although its detailed shape at smaller scales continues to change with increasing κ. The limiting profile is close to the one observed for $\kappa = 11$ (bottom panel).

Figure 4 further illustrates the model instabilities. It shows the period P and maximal value M in 2D sections of the model parameter space.

3.3 Phase locking of the extrema

A distinctive feature of the warm ENSO phase, *i.e.* of an El-Niño event, is its occurrence during a boreal winter. We study here the temporal location of the global maximum and global minimum of solutions, as well as of their local extrema. The key result here is that practically all the extrema of our model solutions occur exclusively within a particular time interval of the seasonal cycle.

The positions of the local extrema (phases) were analyzed for tens of thousands of individual solutions of the model (2)-(3), spanning the entire parameter region $\{(b, \tau) : 0 < b \leq 10,\ 0 < \tau \leq 2\}$, at different values of κ. This analysis was carried out — like that in [20], as summarized in Figs. 2–4 here — when the solutions had settled into their asymptotic behavior, *i.e.* after a sufficiently long transient. The representative results are summarized in Fig. 5, where we used 10 000 individual solutions for each value of κ. The phase variable φ was normalized to lie between 0 and 1, with 0 at the time of year when the trade winds are strongest, *i.e.* close to the first day of October.

The phenomenon of phase locking of the extrema is present for most combinations of the physically relevant model parameters. Moreover, the local maxima tend to occur,

depending on the value of τ, at $\varphi = 0.23$ (late December) or $\varphi = 0.27$ (early January), while the local minima occur at $\varphi = 0.73$ (late June) and $\varphi = 0.77$ (early July).

We notice that the seasonal forcing in our model vanishes at $\varphi = 0.25$ (January 1) and $\varphi = 0.75$ (July 1); hence the local maxima occur in the vicinity of zero forcing when the latter decreases, and the local mimina occur in the vicinity of zero forcing when the latter increases. This corresponds to the local maxima occurring in the model shortly after Christmas, like the observed El Niños, but the model La Niñas are in phase opposition, rather than close to the same season, as they are in the observations. The offset of the position of the extrema from the point of zero external forcing seems to be independent of the model parameters, and the double peaks in the histogram become sharper as the coupling parameter κ increases.

3.4   Multiple solutions

The analysis so far, in [20] and in the previous subsections of this paper, has been done for the model (2)-(3) with fixed history, $\phi(t) \equiv 1$. We now study the dependence of model solutions on distinct, yet still constant histories $\phi(t) \equiv \phi_0$.

Distinct values of the initial history result in distinct model solutions; this is illustrated in Fig. 6 for the parameter values $b = 1$, $\tau = 0.5$, and $\kappa = 10$. To produce this figure we used 20 distinct initial constant histories, uniformly distributed between $\phi_0 = -2$ and $\phi_0 = 2$; at the time $t = 0$ there are thus 20 distinct trajectories. As time passes, those trajectories are attracted by several stable model solutions so that, by $t = 15$, there are only four distinct trajectories left.

We concentrate next on the stable solutions' domains of attraction. Figure 7 shows the model solutions, after transient behavior has decayed, for $-10 \leq \phi_0 \leq 10$, at two points in the model's parameter space: $A = (b = 2, \tau = 0.4, \kappa = 11)$ in the top panel, and $B = (b = 1, \tau = 0.5, \kappa = 10)$ in the bottom panel. Model solutions at point B were illustrated in Fig. 6. At point A, the model has a unique stable solution, which attracts all initial trajectories as time evolves; thus the solution "profile" is constant along any vertical line in the figure's "Hovmoeller diagram.".

At point B, the model has several distinct stable solutions. Recall from Sect. 2.2 that the solutions, and hence their basins of attraction, lie in the function space $X = C([-\tau, 0), \mathbb{R})$. The boundaries of these basins appear in Fig. 7 as horizontal discontinuities in the solution profiles.

There are 8 horizontal discontinuities in the profiles and so there appear to exist 9 attraction basins; as seen in Fig. 6, these 9 basins correspond in fact to only four

asymptotic solutions. Moreover, two of these four can, in turn, be obtained from the other two solutions by a time shift (not shown). The basins of attraction for these two solutions are unions of subintervals of different lengths of the interval $\{\phi_0 : -2 \leq \phi_0 \leq 2\}$, at least when considering, as we have done here, only the subset of our function space X generated by constant initial histories.

Recall, moreover, that Proposition 1 implies that a discontinuity in the solution profile at ϕ_0 suggests that there exists an unstable solution at $\phi(t) \equiv \phi_0$. Hence, the boundaries of the domains of attraction correspond, in all likelihood, to unstable model solutions. Figure 7 suggests the existence of eight unstable solutions; the number of distinct unstable solutions may indeed be less than that.

4 Discussion

In the present paper we reviewed and studied in greater depth a highly idealized model for ENSO variability that is governed by a delay differential equation (DDE) with a single, fixed delay and additive periodic forcing [20]. The use of DDE models to better understand basic ENSO mechanisms was pioneered by Suarez and Schopf [43], Battisti and Hirst [3], and Tziperman et al. [45], following their application to paleoclimate studies by Bhattacharya et al. [4]; see [37] for a comprehensive discussion. Such simple DDE models necessarily ignore a multitude of actual physical mechanisms and processes that might affect ENSO dynamics, as discussed in further detail in [20]. Even so, these models have been shown to successfully capture complex phenomena found in much more detailed ENSO models, including fully coupled global climate models (GCMs), as well as in observational data sets [18].

Given the obvious interest of these simple DDE models, we performed for the first time, to the best of our knowledge, a stability analysis of model solutions in a broad region of the 3-D space of its physically relevant parameters: oceanic wave delay τ, ocean-atmosphere coupling strength κ, and seasonal forcing amplitude b [20]. We found spontaneous transitions in mean thermocline depth, and hence in the sea surface temperature (SST), as well as in the solutions' extreme annual values; these transitions occur for purely periodic, seasonal forcing. Our model, governed by Eqs. (2) and (3), generates intraseasonal oscillations of various periods and amplitudes, as well as interdecadal variability; see Fig. 2.

A sharp neutral curve in the $(b - \tau)$ plane separates smooth parameter dependence in the model's map of "climate metrics" [14, 44] from "rough" behavior; see Figs. 3 and

4 here. We expect such separation between regions of smooth and rough dependence of solution metrics on parameters in much more detailed and realistic models, where it is harder to describe its causes as completely.

The novelty of the present paper, with respect to Ghil *et al.* [20], lies in its focus on multiple model solutions, as a function of initial data, and on the phase locking of local extrema with respect to the seasonal cycle. We found that our DDE model is characterized by the property of its solutions having *extrema* that lock to a particular *phase* φ of the seasonal cycle: the local maxima tend to occur one quarter after the most intense trade winds, *i.e.* in boreal winter, while the local minima tend to occur one quarter after the least intense trades, *i.e.* in boreal summer; see Fig. 5.

As mentioned in the introduction, phase locking of warm events to boreal winter is a main feature of the observed El-Niño events, to the point of having given them their name [11, 40]. At the same time, for small to intermediate seasonal forcing b the position of the global maxima and minima appears to be highly sensitive to changes in parameter values: it may have significant jumps in response to vanishingly small changes in these values.

In reality, both warm (El Niño) and cold (La Niña) events lock to boreal winter, although the cold events are not only less intense [28], but also somewhat less sharply phase locked than the warm ones. It is not clear at this point which one of the lacking features of our DDE model gives rise to this unrealistic phase opposition, and we do mean to explore this matter further. On the other hand, even GCMs with many more detailed features may have their warm events in entirely the wrong season (*e.g.* [18]).

An additional interesting feature of our model, though, is the bimodality of the histogram for the phases of both warm and cold events; see again Fig. 5. Similar bi- or multi-modality of phase locking has been documented in both ODE models of ENSO and in much more realistic, so-called intermediate models [38]. A possible reason for such an effect may lie in the phase locking mechanism itself: as a model solution on the Devil's staircase [26, 45] in parameter space "tries to adapt" to a particular integer multiple of the forcing period from below, it winds up short of the preferred phase, while it will wind up above that phase if its period is originally longer than the integer multiple it tries to achieve (J. D. Neelin, pers. commun., 2009).

Our simple model suggests that the multiple modes of the phase histogram in Fig. 5 are separated by the phase at which the seasonal forcing disappears, and that the sharpness of each mode increases with the strength of the atmosphere-ocean coupling κ. It would be interesting to check whether similar behavior occurs in more detailed models,

as well as in observations.

We found coexistence of multiple stable and unstable solutions for a wide range of model parameters; see Figs. 6 and 7. Typically, each stable solution has its own basin of attraction, which we have explored in the subspace of solutions generated by constant initial histories $\phi(t) \equiv \phi_0$. In this subspace, we have found a finite and, actually, small numbers of stable solutions; some of these, in turn, could be simply obtained from others via a phase shift by an integer number of years. We will further analyze this property in a future study. The boundaries of the attractor basins in Fig. 7 suggest the existence of unstable solutions; their number is probably finite and comparable to the number of distinct stable solutions.

To summarize, the timing of global extrema — *i.e.*, the hottest El Niños and coldest La Niñas — of our simple ENSO model is highly sensitive to the model's parameter values for a wide range of these values. But the local maxima and minima are locked to particular phases of the seasonal cycle. Multiple stable and unstable solutions exist, and the latter seem to play a key role in separating the attractor basins of the former.

Ghil *et al.* [19] and McWilliams [35] have recently discussed the implications of *structural stability* [1] for climate models. The lack thereof is clearly a reason for difficulties in predicting extreme events, like the largest El Niños, sufficiently far in advance; see also [16, 24]. Ghil and co-authors [19] showed, though, that taking into account random perturbations can, in some simple models at least, lead to greater robustness of model behavior. We are planning to study such *stochastic structural stability* effects in our "toy" model as well.

References

[1] Andronov, A. A. and Pontryagin, L. S.: Systèmes grossiers, Dokl. Akad. Nauk SSSR, 14(5), 247–250, 1937.

[2] Battisti, D. S.: The dynamics and thermodynamics of a warming event in a coupled tropical atmosphere/ocean model, J. Atmos. Sci., 45, 2889–2919, 1988.

[3] Battisti, D. S. and Hirst, A. C.: Interannual variability in the tropical atmosphere-ocean system: Influence of the basic state and ocean geometry, J. Atmos. Sci., 46, 1687–1712, 1989.

[4] Bhattacharya, K., Ghil, M., and Vulis, I.: Internal variability of an energy-balance model with delayed albedo effects, J. Atmos. Sci., 39, 1747–1773, 1982.

[5] Bjerknes, J.: Atmospheric teleconnections from the equatorial Pacific, Mon. Wea. Rev., 97, 163–172, 1969.

[6] Boulanger, J.P., Menkes, C., and Lengaigne, M. Role of high- and low-frequency winds and wave reflection in the onset, growth and termination of the 1997-1998 El Nino. Climate Dyn., 22, 2-3, 267–280, 2004.

[7] Cane, M., Munnich, M., and Zebiak, S. E.: A study of self-excited oscillations of the tropical ocean-atmosphere system. Part I: Linear analysis, J. Atmos. Sci., 47 (13), 1562–1577, 1990.

[8] Chang, P., Wang, B., Li, T. and Ji, L.: Interactions between the seasonal cycle and the Southern Oscillation: Frequency entrainment and chaos in intermediate coupled ocean-atmosphere model, Geophys. Res. Lett., 21, 2817–2820, 1994.

[9] Chang, P., Ji, L., Wang, B., and Li, T.: Interactions between the seasonal cycle and El Niño - Southern Oscillation in an intermediate coupled ocean-atmosphere model, J. Atmos. Sci., 52, 2353–2372, 1995.

[10] Delcroix, T., Eldin, G., McPhaden, M., and Morlière, A.: Effects of westerly wind bursts upon the western equatorial Pacific Ocean, February-April 1991, J. Geophys. Res., 98 (C9), 16 379–16 385, 1993.

[11] Diaz, H. F. and Markgraf, V. (Eds.): El Niño: Historical and Paleoclimatic Aspects of the Southern Oscillation, Cambridge Univ. Press, New York, 1993.

[12] Dijkstra, H. A.: Nonlinear Physical Oceanography: A Dynamical Systems Approach to the Large Scale Ocean Circulation and El Niño, 2nd edition, Springer-Verlag, 2005.

[13] Dijkstra, H.A. and Ghil, M.: Low-frequency variability of the ocean circulation: a dynamical systems approach, Rev. Geophys., 43, RG3002, doi:10.1029/2002RG000122, 2005.

[14] Fuglestvedt, J.S., Berntsen, T. K., Godal, O., Sausen, R., Shine, K. P., and Skodvin, T.: Metrics of climate change: Assessing radiative forcing and emission indices, Climatic Change, 58, 267–331, 2003.

[15] Gebbie, G., Eisenman, I., Wittenberg, A., and Tziperman, E.: Modulation of westerly wind bursts by sea surface temperature: A semistochastic feedback for ENSO, J. Atmos. Sci., 64, 3281–3295, 2007.

[16] Ghil, M., and N. Jiang: Recent forecast skill for the El Nio/Southern Oscillation. Geophys. Res. Lett., 25, 171–174.

[17] Ghil, M., Allen, M. R., Dettinger, M. D., Ide, K., Kondrashov, D., Mann, M. E., Robertson, A. W., Saunders, A., Tian, Y., Varadi, F., and Yiou, P: Advanced spectral methods for climatic time series, Rev. Geophys., 40 (1), Art. No. 1003, 2002.

[18] Ghil, M. and Robertson, A. W.: Solving problems with GCMs: General circulation models and their role in the climate modeling hierarchy, In D. Randall (Ed.) General Circulation Model Development: Past, Present and Future, Academic Press, San Diego, 285–325, 2000.

[19] Ghil, M., M. D. Chekroun, and E. Simonnet: Climate dynamics and fluid mechanics: Natural variability and related uncertainties, Physica D, 237, 2111–2126, doi:10.1016/j.physd.2008.03.036, 2008.

[20] Ghil, M., Zaliapin, I., and Thompson, S.: A delay differential model of ENSO variability: Parametric instability and the distribution of extremes. Nonlin. Proc. Geophys., 15, 417–433.

[21] Glantz, M. H., Katz, R. W., and Nicholls, N. (Eds.): Teleconnections Linking Worldwide Climate Anomalies, Cambridge Univ. Press, New York, 545 pp, 1991.

[22] Hale, J.: Theory of Functional Differential Equations, Springer-Verlag, New-York, 1977.

[23] Harrison, D. E. and Giese, B.: Remote westerly wind forcing of the eastern equatorial Pacific; some model results, Geophys. Res. Lett., 15, 804–807, 1988.

[24] Held, I.M.: The gap between simulation and understanding in climate modeling, Bull. Amer. Meteorol. Soc., 86, 1609–1614, 2005.

[25] Jiang, N., Neelin, J. D., and Ghil, M.: Quasi-quadrennial and quasi-biennial variability in the equatorial Pacific, Clim. Dyn., 12, 101–112, 1995.

[26] Jin, F.-f., Neelin, J. D., and Ghil, M.: El Niño on the Devil's Staircase: Annual subharmonic steps to chaos, Science, 264, 70–72, 1994.

[27] Jin, F.-f., Neelin, J. D., and Ghil, M.: El Niño/Southern Oscillation and the annual cycle: Subharmonic frequency locking and aperiodicity, Physica D, 98, 442–465, 1996.

[28] Kondrashov, D., Kravtsov, S., Robertson, A. W. , and Ghil, M.: A hierarchy of data-based ENSO models, J. Climate, 18, 4425–4444, 2005.

[29] Latif, M., Barnett, T. P., Flügel, M., Graham, N. E., Xu, J.-S., and Zebiak, S. E.: A review of ENSO prediction studies, Clim. Dyn., 9, 167–179, 1994.

[30] Lengaigne, M., Guilyardi, E., Boulanger, J.P., *et al.* Triggering of El Nino by westerly wind events in a coupled general circulation model Climate Dyn., 23, 6, 601–620, 2004.

[31] Madden, R. A. and Julian, P. R.: Description of a 40–50 day oscillation in the zonal wind in the tropical Pacific, J. Atmos. Sci., 28, 702–708, 1971.

[32] Madden, R. A. and Julian, P. R.: Description of global-scale circulation cells in the tropics with a 40–50 day period, J. Atmos. Sci., 29, 1109–1123, 1972.

[33] Madden, R. A. and Julian, P. R.: Observations of the 40–50-day tropical oscillation — A review, Mon. Wea. Rev., 122(5), 814–837, 1994.

[34] McPhaden, M. J., Busalacchi, A. J., Cheney, R., *et al.* The Tropical Ocean-Global Atmosphere observing system: A decade of progress, J. Geophys. Res., 103(C7), 14169–14240, 1998.

[35] McWilliams, J. C., Irreducible imprecision in atmospheric and oceanic simulations, Proc. Natl. Acad. Sci. USA, 104, 8709–8713, 2007.

15

[36] Munnich, M., Cane, M., and Zebiak, S. E.: A study of self-excited oscillations of the tropical ocean-atmosphere system. Part II: Nonlinear cases, J. Atmos. Sci., 48 (10), 1238–1248, 1991.

[37] Neelin, J. D., Battisti, D. S., Hirst AC, et al.: ENSO theory, J. Geophys. Res. - Oceans, 103(C7), 14261–14290, 1998.

[38] Neelin, J. D., Jin, F. F., and Syu, H. H.: Variations in ENSO phase locking, J. Climate, 13, 2570–2590, 2000.

[39] Nussbaum, R. D.: Functional Differential Equations, 1998. Available at `http://citeseer.ist.psu.edu/437755.html`.

[40] Philander, S. G. H.: El Niño, La Niña, and the Southern Oscillation, Academic Press, San Diego, 1990.

[41] Saynisch, J., Kurths, J., and Maraun, D.: A conceptual ENSO model under realistic noise forcing, Nonlin. Proc. Geophys., 13, 3, 275–285, 2006.

[42] Shampine, L. F. and Thompson, S.: A friendly Fortran 90 DDE solver, Appl. Num. Math., 56, (2-3), 503–516, 2006.

[43] Suarez, M. J. and Schopf, P. S.: A delayed action oscillator for ENSO, J. Atmos. Sci, 45, 3283–3287, 1988.

[44] Taylor, K. E.: Summarizing multiple aspects of model performance in a single diagram, J. Geophys. Res., 106, 7183–7192, 2001.

[45] Tziperman, E., Stone, L., Cane, M., and Jarosh, H.: El Niño chaos: Overlapping of resonances between the seasonal cycle and the Pacific ocean-atmosphere oscillator, Science, 264, 72–74, 1994.

[46] Tziperman, E., Cane, M. A., and Zebiak, S. E.: Irregularity and locking to the seasonal cycle in an ENSO prediction model as explained by the quasi-periodicity route to chaos, J. Atmos. Sci., 50, 293–306, 1995.

[47] Verbickas, S.: Westerly wind bursts in the tropical Pacific, Weather, 53, 282–284, 1998.

[48] Zebiak, S. and Cane, M. A.: A model El-Niño Southern Oscillation, Mon. Wea. Rev., 115, 2262–2278, 1987.
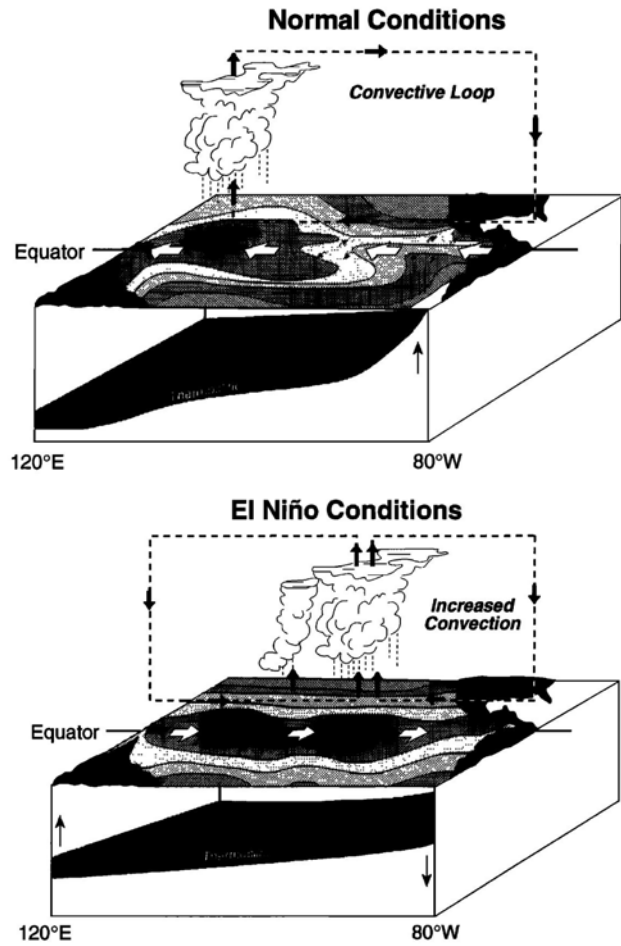
Figure 1: Schematic diagram of the atmospheric and oceanic circulation in the Tropical Pacific. Upper panel: climatological mean ("normal"), lower panel: El Niño (warm) phase. The three-dimensional diagrams show the deepening of the thermocline near the coast of Peru during the warm phase, accompanied by anomalous surface winds (heavy white arrows), modified Walker circulation (lighter black arrows), and a displacement and broadening of the warmest SSTs from the "warm pool" in the western Tropical Pacific, near Indonesia, towards the east. Reproduced from [34], with kind permission of the American Geophysical Union (AGU).

17
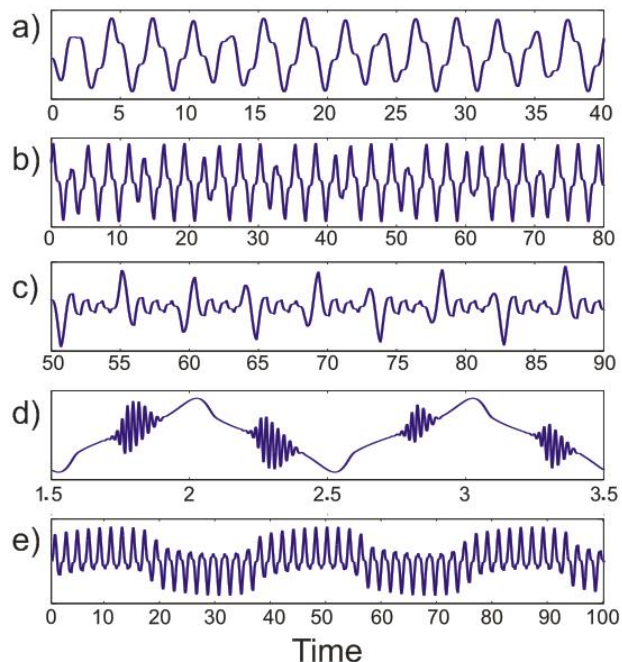
Figure 2: Noteworthy solution patterns of relevance to ENSO dynamics; seasonal forcing amplitude $b = 1$. a) Regularly occurring cold (low-h) events, or La Niñas ($\kappa = 5$, $\tau = 0.65$); b) irregular cold events ($\kappa = 100$, $\tau = 0.58$); c) irregular alternations of warm (El Niño, high-h) and cold events ($\kappa = 50$, $\tau = 0.42$); d) intraseasonal activity reminiscent of Madden-Julian oscillations or westerly-wind bursts ($\kappa = 500$, $\tau = 0.005$); and (e) interdecadal variability in the annual mean and in the relative amplitude of warm and cold events ($\kappa = 50$, $\tau = 0.508$). Reproduced from [20], with kind permission of Copernicus Publications on behalf of the European Geosciences Union (EGU).

18
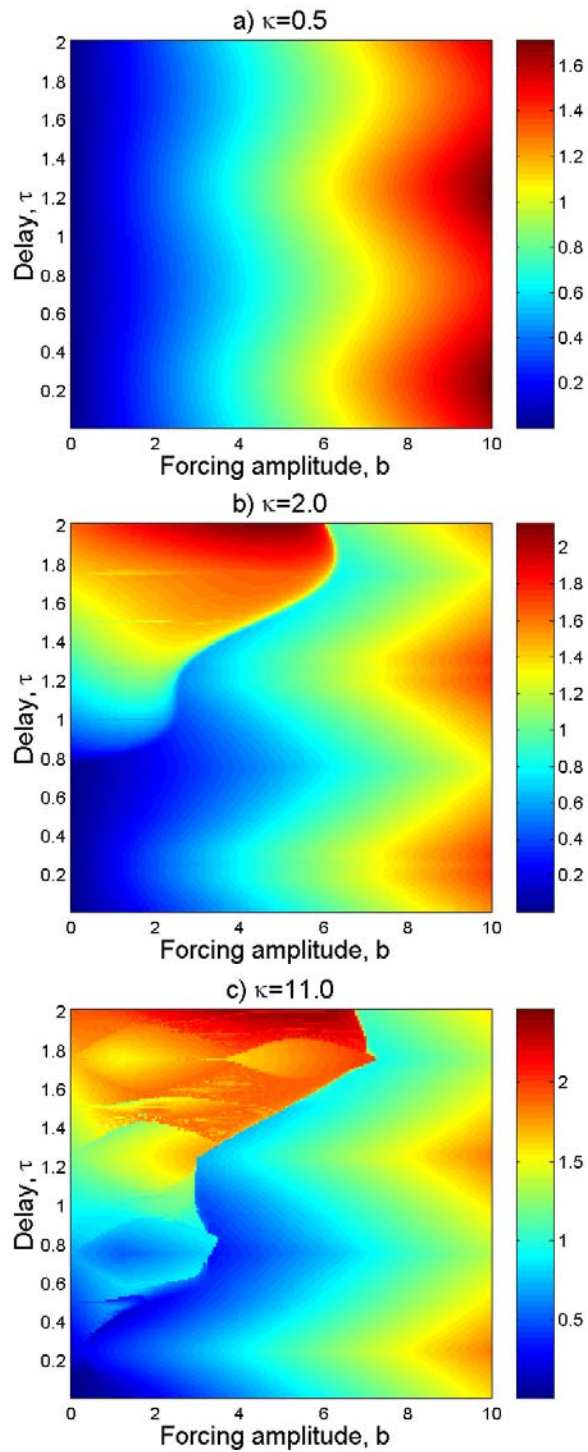
Figure 3: Maximum map $M = M(b, \tau)$. Top: $\kappa = 0.5$, middle: $\kappa = 2$, and bottom: $\kappa = 11$. Notice the onset of instabilities and emergence of a neutral curve $f(b, \tau) = 0$ that separates the smooth from the unstable regions. Reproduced from [20], with kind permission of Copernicus Publications on behalf of the European Geosciences Union (EGU).
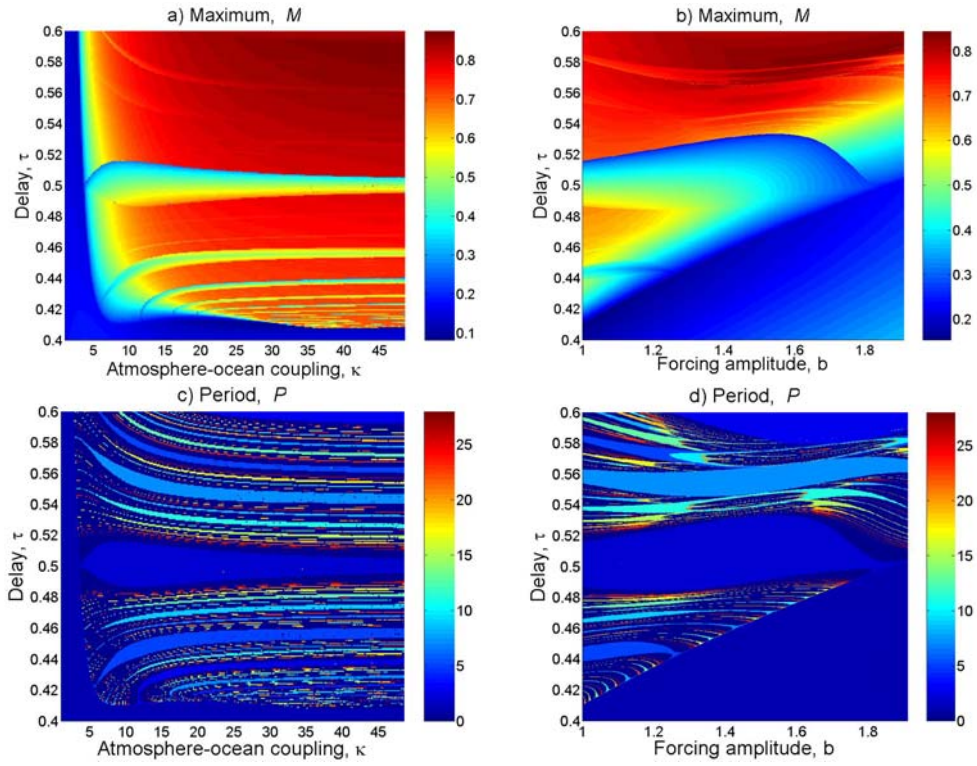
Figure 4: Maximum and period maps. a) Maximum map, $M(\kappa, \tau)$ at $b = 1$; b) Maximum map, $M(b, \tau)$ at $\kappa = 10$; c) Period map, $P(\kappa, \tau)$ at $b = 1$; d) Period map, $P(b, \tau)$ at $\kappa = 10$. Reproduced from [20], with kind permission of Copernicus Publications on behalf of the European Geosciences Union (EGU).
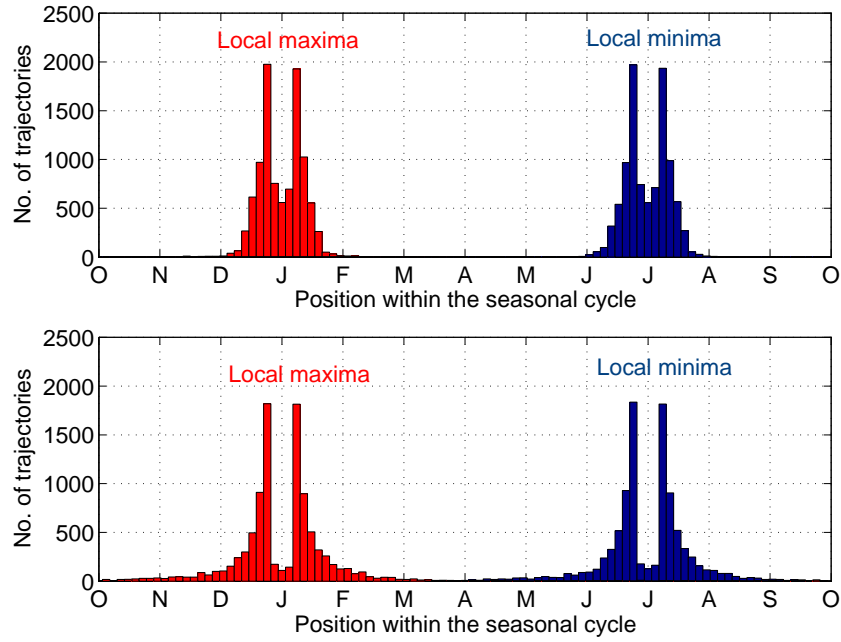
Figure 5: Phase locking of solution extrema: global results. Histogram of the position φ of the global maximum (red bars) and global minimum (blue bars) of solutions of Eq. (2) with $\kappa = 2.0$ (top panel) and $\kappa = 11.0$ (bottom panel). Each panel uses 10 000 individual solutions with parameter values b and τ lying in the ranges $0 < b \leq 10$ and $0 < \tau \leq 2$, respectively.
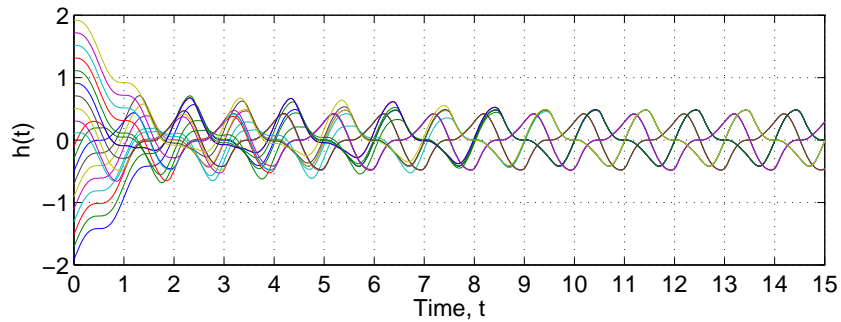
Figure 6: Multiple stable solutions. Twenty trajectories that correspond to as many distinct initial histories $\phi(t) = \phi_0$ collapse, after a transient, onto four stable solutions; these four solutions are indicated by four distinct colors (red, blue, purple and green). Two of these solutions are *distinct*, and the other two can be obtained from the distinct ones by a time shift; notice that a given asymptotic solution, *e.g.* the red one, attracts initial histories that can lie in different segements of the interval $\{\phi_0 : -2 \leq \phi_0 \leq 2\}$. Model parameters are $b = 1$, $\tau = 0.5$, and $\kappa = 10$; see also Fig. 7.

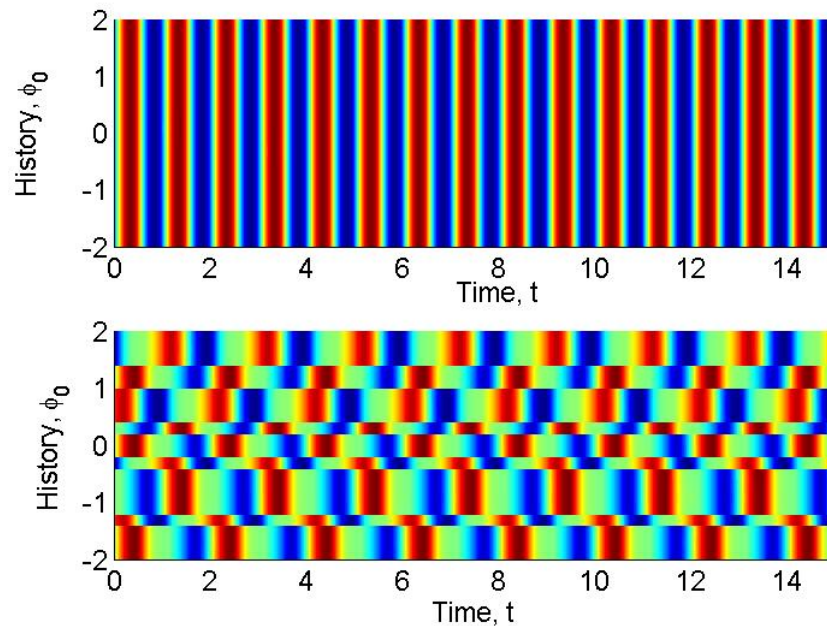Figure 7: Solution profiles for different constant histories $\phi(t) \equiv \phi_0$. Top panel ($b = 2$, $\tau = 0.4$, $\kappa = 11$): there exists a unique stable solution. Bottom panel ($b = 1$, $\tau = 0.5$, $\kappa = 10$; same values as in Fig. 6): there exist several stable solutions, and their basins of attraction are bounded by the horizontal discontinuity lines in the solution profiles; see text for details. The solutions in both panels are shown after a suitably long transient, and the time origin is shifted to start from zero.